Electrical and thermal conductivity of fcc and hcp iron under conditions of the Earth's core from *ab initio* simulations

Uwe Kleinschmidt,[1] Martin French,[1] Gerd Steinle-Neumann,[2] and Ronald Redmer[1]
[1]*Universität Rostock, Institut für Physik, Albert-Einstein-Strasse 23-24, D-18059 Rostock, Germany*
[2]*Bayerisches Geoinstitut, Universität Bayreuth, D-95440 Bayreuth, Germany*

(Received 24 August 2022; revised 14 December 2022; accepted 9 February 2023; published 27 February 2023)

We use *ab initio* simulations based on density functional theory to calculate the electrical and thermal conductivity of solid iron in face-centered cubic and hexagonal phases at high pressures and temperatures up to Earth's core conditions. Both our electrical and thermal conductivities increase systematically with density and reasonably follow the Wiedemann-Franz law, in particular at low temperatures. A trend towards density-independent thermal conductivity observed in recent experiments is not supported by our calculations.

DOI: 10.1103/PhysRevB.107.085145

I. INTRODUCTION

The electrical and thermal conductivity of iron play an important role in the stability and evolution of planetary magnetic fields [1]. Liquid iron dominates the dynamo-active outer core in terrestrial planets, and solid phases in the inner core–at least for Earth and Mercury [2,3]–may influence the generation of magnetic fields [4]. At the high pressure (P) of planetary interiors, experiments show that close-packed phases exist along the melting curve, with the triple point between the face-centered cubic (fcc), the hexagonal close packed (hcp) phases, and the liquid located at $P = 90 - 110$ GPa and temperature $T = 2800 - 3400$ K [5–7]. Despite the lack of experiments indicating its presence [8,9] at conditions of the Earth's core ($P > 135$ GPa and $T \gtrsim 4000$ K [10]), the possible occurrence of the body-centered cubic (bcc) phase predicted by some molecular dynamics simulations [11] remains a topic of debate in mineral physics. However, the consideration of this phase is beyond the scope of the current manuscript.

The past decade has seen significant advances [12–14] in both experimental [15–20] and computational studies [21–31] on high-P conductivities of iron and some of its alloys, but no study has systematically investigated the effect of crystal structure on electronic transport; only the difference between the solid and liquid phases has been considered, for the systematic jump in electrical (σ) and thermal conductivity (λ) [21–23,28]. Here we compare σ and λ of the fcc and hcp phases and explore their anisotropy in the hcp phase. We do so by performing finite-temperature density functional theory (FT-DFT) calculations. This method allows for a description of the electronic and ionic structure of iron from first principles and has been successfully applied also to other metals, e.g., lithium [32], molybdenum [33], and aluminum [34,35].

II. THEORY AND METHODS

A. Density functional theory and molecular dynamics

We describe our system with a combination of FT-DFT [36–38] for the electrons and classical molecular dynamics (MD) for the atoms, based on the Born-Oppenheimer approximation [39], using the Vienna *Ab initio* Simulation Package (VASP) [40–42] in version 5.4.4. Electronic exchange and correlation (XC) effects are approximated with the functional of Perdew, Burke, and Ernzerhof (PBE) [43]. We use a projector augmented wave (PAW) potential [44–46] with 8 valence electrons ([Ar]$4s^1 3d^7$, PAW_PBE Fe_GW) for the electron-ion interaction, and a plane-wave cutoff of 1200 eV. The electronic wave functions are calculated at the Γ point for the hexagonal structure and at the Baldereschi mean value point [47] for fcc. For convenience, an orthorhombic supercell is used to describe the hexagonal structure [48], which yields equivalent results [49]. Temperature is controlled by a Nosé-Hoover thermostat [50,51]. All FT-DFT-MD simulations are performed with a time step of 2 fs and are run for 2–10 ps. Most of these numerical parameters were also used in previous work [29] and we confirm them to yield converged results. We run our simulations at densities $\rho = 9.00, 10.36, 12.00, 13.55$ g/cm^3 and $T = 1850, 3350, 4350, 6350$ K. We carefully monitor the structures through the pair distribution function during the MD simulations to see whether they remain solid and stay in the same symmetry.

Our present calculations exclusively employ the spin-degenerate version of DFT, and calculations in the liquid phase show that this approximation is physically reasonable at $P > 50$ GPa ($\rho \sim 9.5$ g/cm^3), where liquid iron loses its paramagnetic properties [29].

B. Electronic transport coefficients

From each of the equilibrated FT-DFT-MD simulations, we take 10–30 uncorrelated ionic configurations and run static FT-DFT calculations to compute the electronic transport properties, and average the results over configurations. We evaluate the following expressions for the Onsager coefficients derived from linear response theory [52,53]:

$$L_n(\omega) = \frac{2\pi(-1)^n}{V\omega} \sum_{\mathbf{k}\nu\mu} \mathrm{Re}(\langle \mathbf{k}\nu|\hat{\mathbf{v}}|\mathbf{k}\mu\rangle \otimes \langle \mathbf{k}\mu|\hat{\mathbf{v}}|\mathbf{k}\nu\rangle)$$
$$\times (f_{\mathbf{k}\nu} - f_{\mathbf{k}\mu})\left(\frac{E_{\mathbf{k}\mu} + E_{\mathbf{k}\nu}}{2} - h_e\right)^n$$
$$\times \delta(E_{\mathbf{k}\mu} - E_{\mathbf{k}\nu} - \hbar\omega), \tag{1}$$

with frequency ω, the reduced Planck constant $\hbar$, the volume of the simulation box V, the matrix elements $\langle \mathbf{k}\nu|\hat{\mathbf{v}}|\mathbf{k}\mu\rangle$ with the velocity operator $\hat{\mathbf{v}}$ and Bloch states $|\mathbf{k}\mu\rangle$, energy eigenvalue $E_{\mathbf{k}\mu}$, Fermi occupation number $f_{\mathbf{k}\mu}$ and the enthalpy per electron h_e. The matrix elements $\langle \mathbf{k}\nu|\hat{\mathbf{v}}|\mathbf{k}\mu\rangle$ are calculated from the dipole matrix elements $\langle \mathbf{k}\nu|\hat{\mathbf{r}}|\mathbf{k}\mu\rangle$[1] that take into account the nonlocal contributions from the PAW potentials and are implemented in the optical routines of VASP [53,54]. A Gaussian function is used to broaden the δ function to a small finite width.

The static electrical conductivity is given by

$$\sigma = e^2 \lim_{\omega \to 0} L_0(\omega), \tag{2}$$

where e is the elementary charge. The coefficient $L_0(\omega)$ is known as the ω-dependent Kubo-Greenwood formula [55,56]. The thermal conductivity reads

$$\lambda = \frac{1}{T} \lim_{\omega \to 0} \left(L_2(\omega) - L_1(\omega)L_0^{-1}(\omega)L_1(\omega)\right). \tag{3}$$

In practice, the static electrical and thermal conductivities are derived by linear extrapolations to $\omega = 0$ across an unphysical decrease at very small ω (Fig. 3 in the Supporting Online Material [57]).

The electrical and thermal conductivity are related by the Lorenz number, which is given by

$$L = \frac{\lambda}{T\sigma}\left(\frac{e}{k_B}\right)^2, \tag{4}$$

with the Boltzmann constant k_B. In the degenerate limit, the Wiedemann-Franz law [58,59] describes this ratio between λ and σ by the constant value of $\pi^2/3$ [60].

The static FT-DFT calculations are run with an energy cutoff of 400 eV [29] and several different Monkhorst-Pack **k**-point sets in the irreducible wedges of the Brillouin zones of the ideal crystalline supercells [61], similar to previous work [33,62]. Our convergence tests on particle number and **k** points (see Tables I-III in the Supporting Online Material [57]) show that it is necessary to consider at least 288 atoms and a reduced wedge Monkhorst-Pack **k**-point set of 4 × 4 × 4 in case of the hexagonal (orthorhombic) system and 256 atoms and a reduced wedge Monkhorst-Pack **k**-point set of 4 × 4 × 4 for the fcc structure to get results for σ and λ that are converged to 1–6%, depending on density ρ and T. Further, we quantify the influence of the pseudopotential, which somewhat affects the ionic configurations generated from the FT-DFT-MD simulations and, consequently, conductivities in Figs. 1 and 2 of the Supporting Online Material [57]. Compared to a hard potential with 16 valence electrons, σ is lower by 5% compared to the 8-valence electron potential. Combining these accuracy assessments, we estimate an uncertainty of 10% for the calculated transport properties.

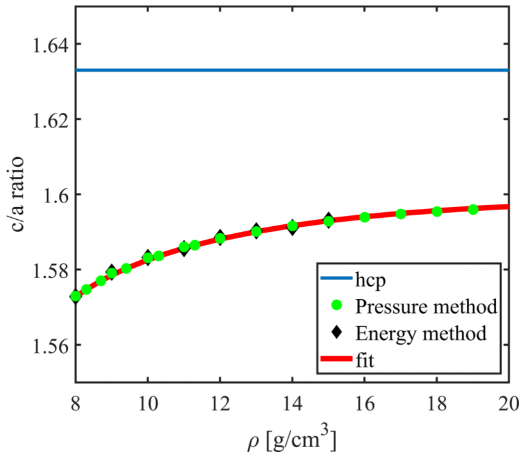

FIG. 1. Dependence of the c/a ratio in hexagonal iron on density at $T = 0$. DFT results are shown as green dots (pressure method) and black diamonds (energy method) compared to the ideal hcp ratio (blue line). Results are fitted (red) with an analytical function, Eq. (5).

C. Static DFT calculations for hexagonal iron

Before discussing the FT-DFT-MD simulations, we examine the equilibrium geometry of hexagonal iron at $T = 0$ with static DFT calculations. By adjusting the c/a ratio at given ρ until the diagonal elements of the pressure tensor are equal, we find hydrostatic ratios for densities between 4.35 and 26.5 g/cm^3, and test this approach by minimizing

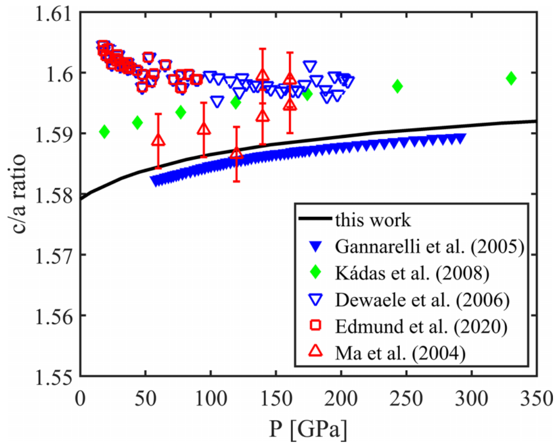

FIG. 2. Static c/a ratios of hexagonal iron calculated in the pressure range up to 350 GPa. Our results from Eq. (5) are shown as a black line, and compared to other DFT calculations by Gannarelli *et al.* [63] (blue triangles) and Kádas *et al.* [65] (green diamonds). Also shown are experimental data at room T by Dewaele *et al.* [66] (open blue triangles), Edmund *et al.* [67] (open red squares), and Ma *et al.* [68] (open red triangles).

---

[1] This procedure is only applicable to the off-diagonal matrix elements. However, diagonal matrix elements (electron velocities) do not contribute in Eq. (1).

TABLE I. Coefficients for Eq. (5).

b_0	b_1 [cm^3/g]	b_2 [(cm^3/g)^2]	b_3 [(cm^3/g)^3]	b_4 [(cm^3/g)^4]
1.591	0.5813	−13.00	88.34	−246.10

total energy as a function of c/a at selected ρ. For these calculations we use a hexagonal cell with two atoms and a Monkhorst-Pack **k**-point mesh of 39 × 39 × 30 and an energy cutoff of 1200 eV, which is sufficient to converge all pressure tensor components.

III. RESULTS

A. c/a ratio at zero temperature

The hydrostatic c/a ratio at $T = 0$ is always smaller than the ideal hcp ratio of $\sqrt{8/3} \approx 1.633$ (Fig. 1). It decreases strongly toward low ρ and approaches a constant value of ∼1.60 for high ρ. Numerically, we fit our results to

$$\frac{c}{a}(\rho, T = 0) = b_0 + \frac{b_1}{\rho} + \frac{b_2}{\rho^2} + \frac{b_3}{\rho^3} + \frac{b_4}{\rho^4}, \qquad (5)$$

with coefficients given in Table I. Results from equalizing the components of the pressure tensor and minimizing energy are fully consistent.

In Fig. 2 we compare our c/a results to other DFT calculations and experimental data at room T. In the range $P = 0 - 350$ GPa, our results are in a good agreement with earlier DFT calculations by Gannarelli *et al.* [63], Steinle-Neumann *et al.* [64], and Kádas *et al.* [65], the latter with a small systematic deviation relative to the other results.

Figure 2 also shows measurements by Dewaele *et al.* [66], Edmund *et al.* [67], and Ma *et al.* [68] at room T, who provide results in the same P region as the DFT calculations. Differences of our results to experiments are likely due to the PBE approximation of the XC functional, assuming $T = 0$, and nuclear vibrational quantum effects not considered here.

In the following, we use the c/a ratio from Eq. (5) as a lower bound in our FT-DFT-MD simulations as the c/a ratio can be expected to increase with T and, possibly, approach the ideal hcp value. Experiments of Ma *et al.* [68] indicate that the T dependence of the c/a ratio is very weak up to 2750 K.

B. Pressure-temperature conditions

An analoguous determination of the hydrostatic c/a ratios for each ρ at various $T > 0$ would require a large amount of FT-DFT-MD simulations, which we did not attempt. Instead, we explore the sensitivity of conductivities on c/a by performing the calculations with three different ratios: The static value from Eq. (5), the ideal value of $c/a = \sqrt{8/3} \approx 1.633$, and $c/a = 1.61$, which lies in between.

Figure 3 shows the P−T conditions generated in our simulations. All hexagonal and the fcc structures result in very similar P at given T and ρ, with differences <7%. For nonhydrostatic conditions, the average of the diagonal components of the pressure tensor is taken as total P.

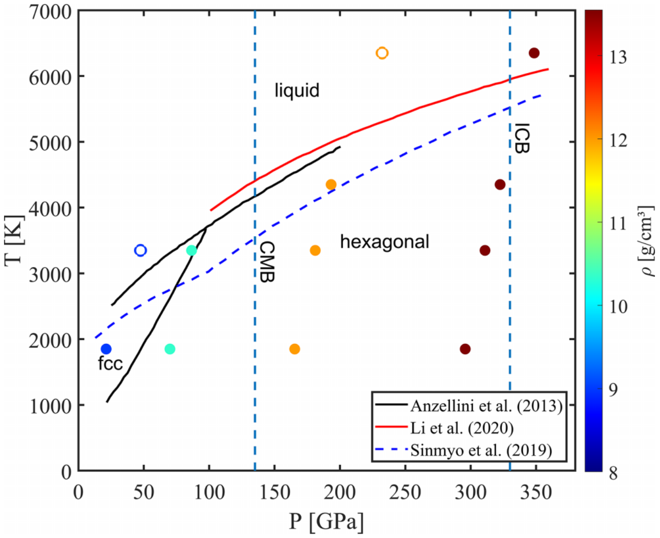

FIG. 3. Phase diagram of iron with phase boundaries given by Anzellini *et al.* [8], Li *et al.* [69], and Sinmyo *et al.* [9]. The symbols show the pressure-temperature conditions for the simulations we perform. Open circles indicate iron in the liquid phase, filled circles the hcp phase. Also shown are the pressures at the core-mantle (CMB) and inner core boundary (ICB) in Earth (dashed vertical lines).

As calculations with the PBE functional do not reproduce the experimental P−ρ relation correctly, we add a P correction from Wagle and Steinle-Neumann [10] to mitigate this inaccuracy. This correction has a more pronounced effect for calculations at $\rho = 9$ g/cm^3, where the correction leads to $P = 9$ GPa compared to 12 GPa obtained directly from the simulations. For higher ρ, the P correction becomes smaller and is almost negligible for our highest ρ values, with 1 GPa on $P = 300$ GPa from FT-DFT-MD.

The pair distribution function and particle diffusion reveals that the solid structures melt into the liquid state at two conditions ($\rho = 9$ g/cm^3, $T = 3350$ K and $\rho = 12$ g/cm^3, $T = 6350$ K), generally consistent with experimental melting curves (Fig. 3). Those simulations are excluded from further processing.

Based on a decrease of the pressure tensor anisotropy at higher c/a ratio for high T, we infer that the hydrostatic c/a ratio has to increase with T at given ρ. Nevertheless, the hydrostatic c/a ratios at arbitrary T fall between the value calculated for $T = 0$ (Fig. 1) and the ideal hcp value.

C. Conductivity anisotropy in hcp iron

Our computed electrical and thermal conductivity tensors show that they are relatively insensitive to the c/a ratio, especially for $T \geqslant 3350$ K (Tables IV and V in the Supporting Online Material [57]). Due to the small influence of c/a on conductivities, we continue the discussion exclusively for the conductivities of ideal hcp (Figs. 4 and 5). Because of the hexagonal symmetry, the xx and yy components of the conductivity tensors, i.e., in the basal plane (indexed with B) should be equal, which we observe within 4–5% for our orthorhombic supercells with 288 atoms (Tables I and II in the Supporting Online Material). This small deviation supports the good convergence with respect to **k** points and particle numbers in our calculations, and we take the mean values of the xx and yy components as σ_B and λ_B.

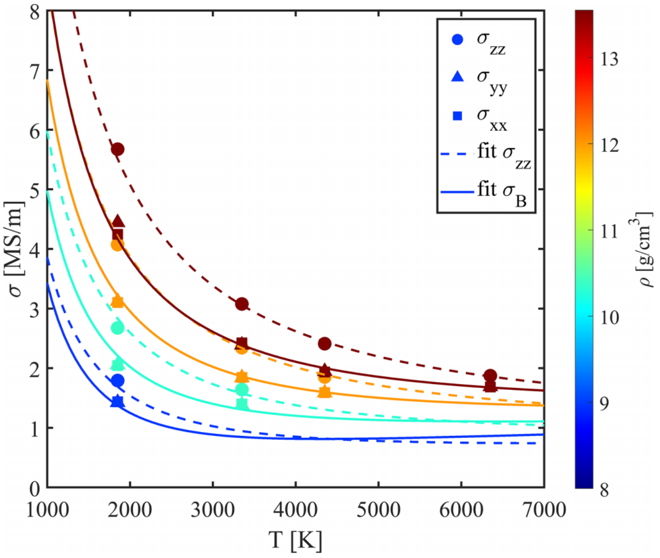

FIG. 4. Components of the electrical conductivity tensor for hcp Fe, σ_{xx} (squares), σ_{yy} (triangles), and σ_{zz} (circles), for different temperature and densities from simulations with 288 atoms. Also shown are fits for σ_{zz} (dashed lines) and σ_B (solid lines) using Eq. (6).

The zz component of σ and λ in the hexagonal phase is systematically larger by 3–33% than the basal component. The magnitude of the anisotropy decreases with T and almost vanishes at 6000 K. Anisotropy in conductivities for hcp iron has previously been reported by Xu *et al.* [27] and Ohta *et al.* [70]. Xu *et al.* [27] predicted $\sigma_{zz} > \sigma_{xx}$ with a combination of DFT and dynamical mean-field theory (DFT+DMFT) by a factor of 1.3, comparable to our results. Ohta *et al.* [70] measured $\lambda_{zz} > \lambda_B$ by a factor of 3–4 at room T, in line with the T trend of the anisotropy, although with a significantly larger value.

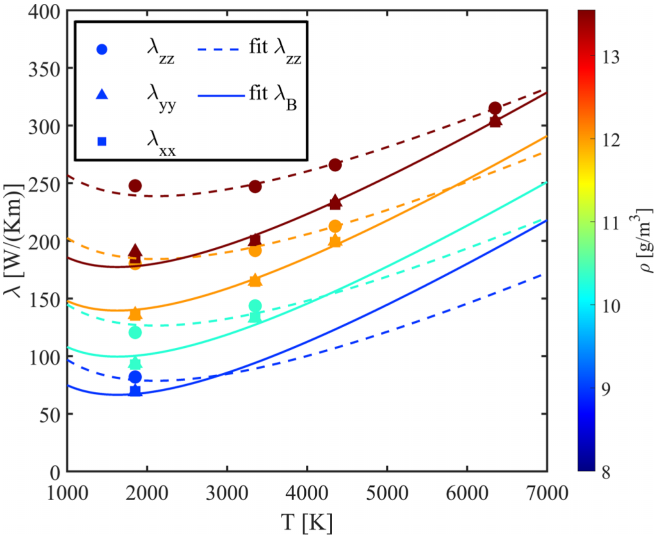

FIG. 5. Components of the thermal conductivity tensor for hcp Fe, λ_{xx} (squares), λ_{yy} (triangles), and λ_{zz} (circles), for different temperature and densities from simulations with 288 atoms. Also shown are fits for λ_{zz} (dashed lines) and λ_B (solid lines) using Eq. (7).

TABLE II. Coefficients for Eq. (6).

	$T\sigma_{\rm fcc}$	$T\sigma_B$	$T\sigma_{zz}$
c_0 [MSK/m]	−2477	17490	7464
c_1 [SKm^2/g]	1434	1136	1555
c_2 [MS/m]	0.933	1.684	1.101
c_3 [MSK/m]	−1228	−3760	−2708

D. Comparison of hcp and fcc conductivities

Results for the basal plane B and zz components of σ and λ are used for analytical fits. The following expressions, which allowed for an accurate parametrization of FT-DFT-MD conductivity data for solid molybdenum [33], are used:

$$T\sigma_i = c_0 + c_1\rho + c_2 T + c_3 \ln T, \tag{6}$$

$$\lambda_i = d_0 + d_1\rho + d_2 T + d_3 \ln T. \tag{7}$$

Resulting coefficients are given in Tables II and III. Computed conductivities for fcc iron are processed the same way. These fit formulas are purely empirical and should not be extrapolated far beyond the underlying points used in the parametrization.

In Fig. 6 we show electrical conductivities in the fcc phase compared with the directionally averaged values for the hcp phase calculated via

$$\sigma_{\rm hcp} = \tfrac{2}{3}\sigma_B + \tfrac{1}{3}\sigma_{zz}. \tag{8}$$

The electrical conductivity decreases with T and increases with ρ, and values for the fcc structure are larger than for hcp by up to ∼25%. Also shown are plots of the fit functions, Eq. (6), along isotherms which reproduce the numerical results very well.

For the thermal conductivity, averaging was done the same way as for σ, see Eq. (8), and results are shown in Fig. 7. The thermal conductivity increases with T and ρ for both structures, and–as for σ–the values in the fcc structure are systematically larger by up to ∼25%. The fit curves from Eq. (7) are in a good agreement with the computational results. Intersections between them at low T are probably artificial and should be viewed with caution.

E. Lorenz number

Figure 8 shows the Lorenz number calculated from Eq. (4) using our conductivity results. The Lorenz number of hcp and fcc iron decreases with P and increases with T. At low T the results for L become nearly constant and agree with the Wiedemann-Franz law [58,59] $L = \pi^2/3$, within few percent.

TABLE III. Coefficients for Eq. (7).

	$\lambda_{\rm fcc}$	λ_B	λ_{zz}
d_0 [W/(Km)]	−137.1	373	315.8
d_1 [10^{-6}Wm^2/(gK)]	35.29	24.35	35.19
d_2 [W/(K^{2}m)]	0.02538	0.05051	0.03958
d_3 [W/(Km)]	−20.07	−82.2	−83.27

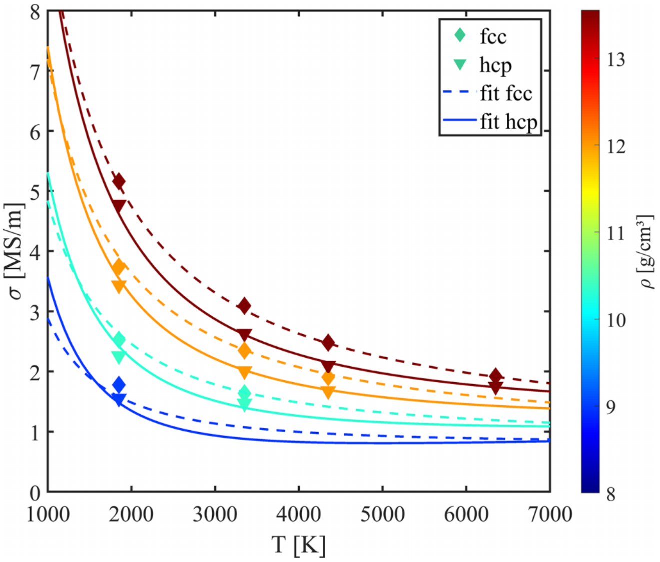

FIG. 6. Dependence of electrical conductivity on temperature for given densities for solid iron phases. Results for hcp Fe (triangles) are compared to those of the fcc phase (diamonds). Fits from Eq. (6) are shown as solid lines for hcp and dashed lines for fcc.

The T and P dependence of L is somewhat weaker for the fcc phase than for hcp. At high T, the Lorenz number shows significantly positive deviations from the Wiedemann-Franz law that can exceed 10%.

Within the adiabatic approximation, the Wiedemann-Franz law can be derived from kinetic theory for a fully degenerate electron gas, regardless of the scattering mechanisms of the electrons or complexity of electronic structure [60]. The deviations in our calculations likely arise from thermal electronic excitations and increasing lattice disorder in the ionic structure. They cannot be caused by electron-electron collisions, which our method does not account for as DFT represents a single-particle approximation of electrons [71]. Note that in liquid iron, where electrons are less degenerate, FT-DFT-MD calculations reproduce experimental data for σ and λ along a low-P isobar within 10%, while also closely following the Wiedemann-Franz law [29]. This suggests that electron-electron scattering is not an important process in iron at geophysical relevant conditions. Electron-electron scattering must not be confused with correlations among electrons, which are important and are approximated with the PBE XC functional used in our work.

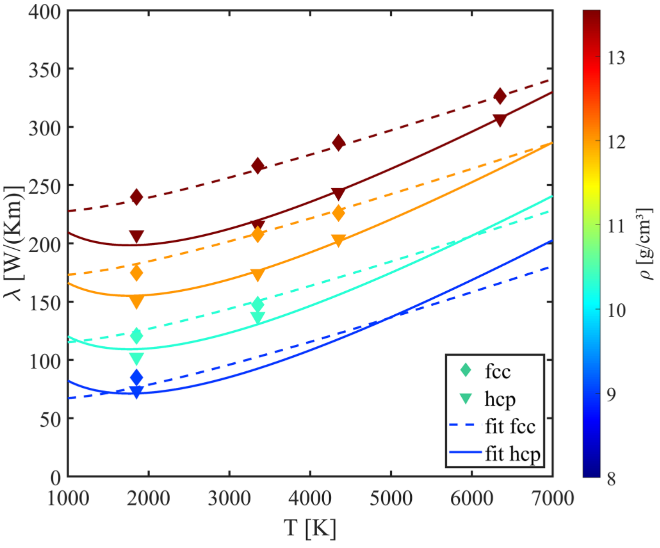

FIG. 7. Dependence of thermal conductivity on temperature for given densities for solid iron phases. Results for hcp Fe (triangles) are compared to that of the fcc phase (diamonds). Fits from Eq. (7) are shown as solid lines for hcp and dashed lines for fcc.

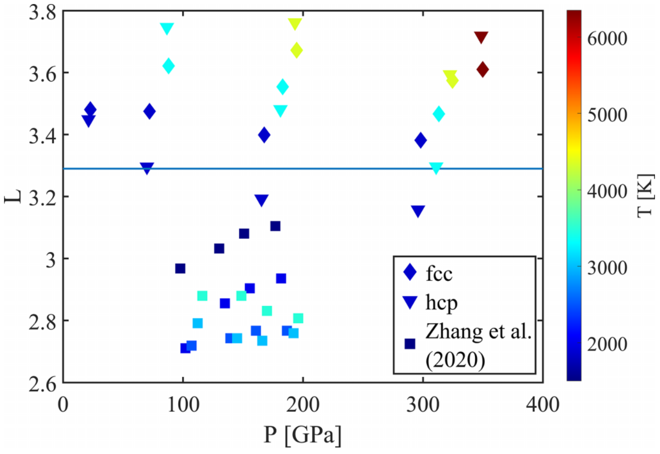

FIG. 8. Lorenz number for iron at high pressure and temperature. Our results for the hcp (triangles) and fcc (diamonds) phases are compared to those from Zhang *et al.* [20] for hcp iron (squares) using DFT+DMFT. The line indicates the degenerate limit $L = \pi^2/3$ from the Wiedemann-Franz law.

IV. DISCUSSION

A. Comparison of conductivities with other computations and experiments

In Fig. 9, our FT-DFT-MD results for σ_{hcp} are compared to those of Pozzo *et al.* [23,24], who applied the same computational approach along two isochores. At $\rho = 10.36\ \text{g/cm}^3$ ($P < 100$ GPa) our simulations reproduce the values of Pozzo and Alfè [24] very well. Larger systematic differences occur for $\rho = 13.55\ \text{g/cm}^3$ (in the 300 GPa region), where both our P and conductivities are lower by 3–10%. While this is within the stated uncertainity of our results, the difference is systematic and warrants further consideration that may hint at possible causes:

(i) We find that the pressure tensor is not converged when using an energy cutoff of 293 eV as in Ref. [24].

(ii) In some cases we observe that if FT-DFT-MD simulations for hcp iron start with configurations too far from equilibrium, structural distortions of the lattice (especially in the third coordination shell) can occur, which then lead to inconsistent values in the pressure tensor, for σ, and for λ.

(iii) The extrapolation of $\sigma(\omega)$ to $\omega = 0$ may arrive at different results, with the linear extrapolation used here (Fig. 3 in the Supporting Online Material [57]) sometimes leading to larger values than a Drude fit used elsewhere [21].

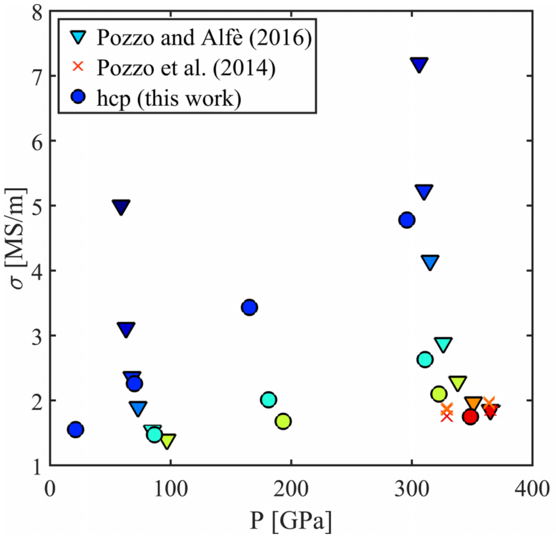

FIG. 9. Electrical conductivity of hcp iron as a function of pressure and temperature. Our results (circles) are compared to those from Pozzo *et al.* [23,24] (triangles and diamonds) in the same T and P range.

To compare our conductivity results to experimental data at arbitrary P and T, we use the Birch-Murnaghan equation of state for hcp iron by Belonoshko [73] to determine the P corresponding to our fit curves for $\sigma(\rho, T)$ and $\lambda(\rho, T)$. Resulting isothermal curves for the electrical and thermal conductivity as a function of P are compared with diamond anvil cells measurements in Figs. 10 and 11.

The electrical conductivity is compared to high-T experiments by Ohta *et al.* [17] and Zhang *et al.* [20], and a model resulting from experiments at room T by Gomi *et al.* [15] in Fig. 10. Both experimental and computed σ increase with P and decrease with T. The data of Zhang *et al.* [20] agree very well with our values at low P; however, they diverge for higher P as our σ rises much less steeply than theirs. Gomi *et al.* [15] tabulated values for σ at selected geophysically interesting points, like the core-mantle boundary (CMB) and inner core boundary (ICB). Their extrapolations to 101 GPa and 2010 K and the CMB (135 GPa and 3750 K) agree well with our isothermal model curves at 1850 K and 3350 K; larger deviations occur for high P and T extrapolations, at 208 GPa and 5220 K and P at the ICB (330 GPa and 4971 K). Values for σ by Ohta *et al.* [17] are significantly higher than ours for all P-T conditions of their experiments. Lobanov and Geballe [72] suggest that the large discrepancies between experimental results may originate from P-induced changes of sample geometry; they semiquantitatively reanalyzed experimental data by Ohta *et al.* [17] and Zhang *et al.* [20], and found that the discrepancy between the measurements decrease, as well as the difference between our results and experimental data.

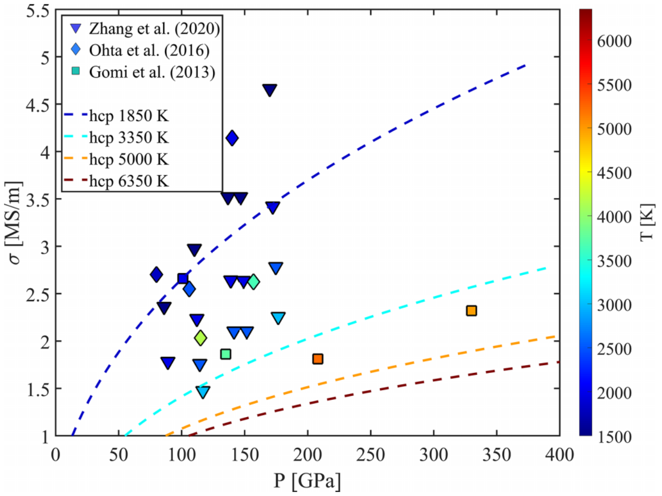

FIG. 10. Electrical conductivity of hcp iron as a function of pressure for given temperature. Our fit is shown as dashed lines for four isotherms and compared to experimental data of Zhang *et al.* [20] (triangles), Ohta *et al.* [17] (diamonds), and Gomi *et al.* [15] (squares).

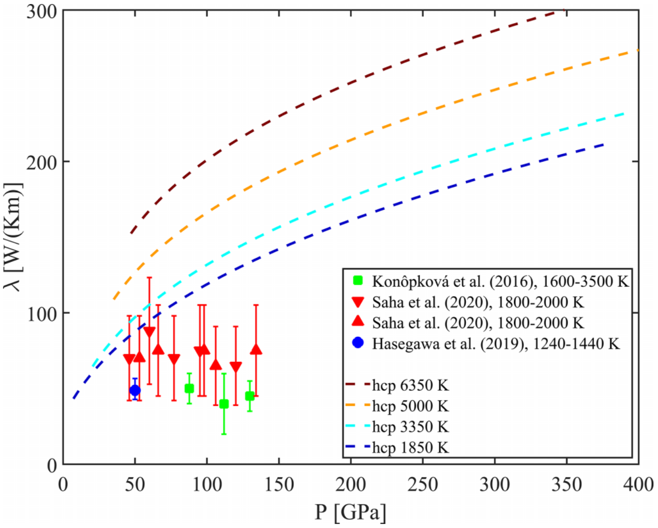

FIG. 11. Thermal conductivity of hcp iron as a function of pressure: Experimental data from Konôpková *et al.* [16] (green squares), Saha *et al.* [19] (red triangles: Upward for pressure transmitting medium NaCl and downward for pressure transmitting medium Al_2O_3), and Hasegawa *et al.* [18] (blue circle) are compared to the fit of our FT-DFT-MD results for hcp iron evaluated along four isotherms.

The thermal conductivity is compared to experiments by Konôpková *et al.* [16], Saha *et al.* [19], and Hasegawa *et al.* [18] in Fig. 11. The values of Saha *et al.* [19] overlap with our curve for 1850 K at low P. Strangely, these measurements show no increase with P unlike our FT-DFT-MD results. This also applies to the measurements of Konôpková *et al.* [16], made for $T = 1600 - 3500$ K, which report much lower values than ours. The data from Hasegawa *et al.* [18] fall in the range of the other two experiments.

B. Lorenz number

A different P dependence for σ and λ would imply a P-dependent Lorenz number, Eq. (4), and consequently a strong departure from the Wiedemann-Franz law at higher P. Since our calculated σ and λ rise similarly with P, we do not observe a substantial P dependence of the Lorenz number (Fig. 8). Further, measured values of σ_{hcp} are generally larger than the FT-DFT-MD results (Fig. 10), whereas the experiments on λ generally yield smaller values (Fig. 11), especially at $P > 100$ GPa. If these combined experimental trends are correct, a Lorenz number smaller by a factor of 2–3 than the Wiedemann-Franz limit of $L = \pi^2/3$ would follow. Such a large deviation would require a special theoretical explanation, especially as the degeneracy of electrons becomes stronger with P, which increasingly favors a Lorenz number *converging to* the Wiedemann-Franz limit, not *diverging from* it.

Zhang *et al.* [20] calculated the Lorenz number with DFT+DMFT using additional repulsive interaction energies between correlated electronic orbitals via Hubbard model parameters U and J that are chosen by external constraints [26,27]. This changes the electronic structure of iron compared to standard DFT calculations and influences σ and λ, also lowering the Lorenz number by up to 20% (Fig. 8). While the DFT+DMFT approach may offer an improved description of electronic correlations, it remains an open question whether it can properly describe electron-electron collisions as claimed previously [25–27]. Further, the DFT+DMFT method has not yet been benchmarked against experiments in the liquid phase [74–78]; neither has the high-T limit for which the exact limit for L that accounts for electron-electron scattering, known from Spitzer theory [71,79], been reproduced with the DFT+DMFT method.

C. Planetary implications

Assuming $T = 6350$ K at the ICB (330 GPa) [10,22], $\sigma = 1.65$ MS/m and $\lambda = 295$ W/(Km) for the hcp phase, making up the Earth's inner core, are juxtaposed with $\sigma = 1.60$ MS/m and $\lambda = 230$ W/(Km) for liquid iron [21], as a first-order approximation to the outer core. The small discontinuity (Δ) in σ between the solid and liquid is in line with systematic considerations by Wagle and Steinle-Neumann [28] based on the Ziman approximation, and slightly smaller than that estimated by Pozzo *et al.* [22–24] ($\Delta\sigma = 0.20$ MS/m). By contrast, the large difference in thermal conductivity with $\Delta\lambda = 70$ W/(Km) between the liquid and solid (with $\Delta\lambda = 90$ W/(Km) by Pozzo *et al.* [22–24] even larger) is of geophysical significance, with direct consequences on the thermal state and deformation regime of the inner core [80]. With a significantly larger value of λ in the inner core, a difference that will even increase [81] by the expulsion of light elements during its solidification from the outer core [80], the inner core is likely not in a convective regime as heat is conducted very efficiently along an adiabat, counteracting the buildup of a superadiabatic T profile that could form as a consequence of a thermal memory effect during its solidification history [82].

The presence of a significant amount of light elements [83] in the core of Mercury and limited knowledge of its internal structure [84,85] makes a similar comparison for the innermost planet in our solar system less meaningful. Nevertheless, at its central $P \sim 40$ GPa [83,86], with the melting point of Fe of ∼2500 K [6], the fcc phase of iron coexists with the liquid, with values for $\sigma = 1.32$ MS/m (1.28 MS/m for the liquid [21]) and $\lambda = 90$ W/(Km) (75 W/(Km) for the liquid [21,28]), respectively. The jump in σ is comparable to that at ICB conditions in the Earth, and significantly smaller than that obtained by Wagle and Steinle-Neumann [28] ($\Delta\sigma = 0.18$ MS/m), putting the applicability of the Ziman approximation for iron at high P used in their work in question.

V. CONCLUSION

We have calculated the electrical σ and thermal conductivities λ of hexagonal and fcc iron at high pressures and temperatures from density functional theory. We show that for the hexagonal phase they display significant anisotropy that decreases with T, although the c/a ratio has little influence on calculated conductivities. Our results for the Lorenz number closely follow the Wiedemann-Franz law, in contrast to trends one may deduce from various recently performed experiments and computations that consider additional electronic repulsion (dynamic mean field theory). In particular, our calculated thermal conductivity is two times larger than experimental values and shows a linear increase with density. Our results for electrical conductivity are in good agreement with experiments at low T and P, but are smaller in the higher $P-T$ region. These discrepancies need to be resolved by future experiments and further computations, possibly on other, simpler, metals. Finally, we provide convenient fit formulas for $\sigma(\rho, T)$ and $\lambda(\rho, T)$ for application in planetary science and comparison to experiments.

ACKNOWLEDGMENTS

We thank Stewart McWilliams for helpful discussions and Georg Kresse for providing us with the Fe_sv_h PAW potential. This work was supported by the Deutsche Forschungsgemeinschaft (DFG) within the Research Unit FOR 2440 and the Priority Program SPP 1992. The *ab initio* calculations were performed at the North-German Supercomputing Alliance (HLRN) facilities and at the IT and Media Center of the University of Rostock.

---

[1] C. Davies, M. Pozzo, D. Gubbins, and D. Alfè, Nature Geosci. **8**, 678 (2015).

[2] P. Cummins and L. R. Johnson, J. Geophys. Res. **93**, 9058 (1988).

[3] A. Genova, S. Goossens, E. Mazarico, F. G. Lemoine, G. A. Neumann, W. Kuang, T. J. Sabaka, S. A. Hauck II, D. E. Smith, S. C. Solomon, and M. T. Zuber, Geophys. Res. Lett. **46**, 3625 (2019).

[4] H. Amit and P. Olson, Earth Planet. Sci. Lett. **414**, 68 (2015).

[5] T. Komabayashi, Y. Fei, Y. Meng, and V. Prakapuka, Earth Planet. Sci. Lett. **282**, 252 (2009).

[6] T. Komabayashi, J. Geophys. Res. Solid Earth **119**, 4164 (2014).

[7] D. Zhang, J. M. Jackson, J. Zhao, W. Sturhahn, E. E. Alp, M. Y. Hu, T. S. Toellner, C. A. Murphy, and V. B. Prakapenka, Earth Planet. Sci. Lett. **447**, 72 (2016).

[8] S. Anzellini, A. Dewaele, M. Mezouar, P. Loubeyreand, and G. Morard, Science **340**, 464 (2013).
[9] R. Sinmyo, K. Hirose, and Y. Ohishi, Earth Planet. Sci. Lett. **510**, 45 (2019).
[10] F. Wagle and G. Steinle-Neumann, J. Geophys. Res. Solid Earth **124**, 3350 (2019).
[11] A. B. Belonoshko, T. Lukinov, J. Fu, J. Zhao, S. Davis, and S. I. Simak, Nat. Geosci. **10**, 312 (2017).
[12] M. Berrada, R. A. Secco, W. Yong, and J. A. H. Littleton, J. Geophys. Res. Planets **125**, e2020JE006380 (2020).
[13] M. Berrada, R. A. Secco, and W. Yong, Sci. Rep. **12**, 9941 (2022).
[14] Y. Yin, L. Wang, S. Zhai, and Y. Fei, J. Geophys. Res. Planets **127**, e2021JE007116 (2022).
[15] H. Gomi, K. Ohta, K. Hirose, S. Labrosse, R. Caracas, M. J. Verstraete, and J. W. Hernlund, Phys. Earth Planet. Inter. **224**, 88 (2013).
[16] Z. Konôpková, R. McWilliams, N. Gómez-Pérez, and A. F. Goncharov, Nature (London) **534**, 99 (2016).
[17] K. Ohta, Y. Kuwayama, K. Hirose, K Shimizu, and Y. Oshishi, Nature (London) **534**, 95 (2016).
[18] A. Hasegawa, T. Yagi, and K. Ohta, Rev. Sci. Instrum. **90**, 074901 (2019).
[19] P. Saha, A. Mazumder, and G. D. Mukherjee, Geosci. Front. **11**, 1755 (2020).
[20] Y. Zhang, M. Hou, G. Liu, C. Zhang, V. B. Prakapenka, E. Greenberg, Y. Fei, R. E. Cohen, and J.-F. Lin, Phys. Rev. Lett. **125**, 078501 (2020).
[21] N. de Koker, G. Steinle-Neumann, and V. Vlček, Natl. Acad. Sci. **109**, 4070 (2012).
[22] M. Pozzo, C. Davies, D. Gubbins, and D. Alfè, Nature (London) **485**, 355 (2012).
[23] M. Pozzo, C. Davies, D. Gubbins, and D. Alfè, Earth Planet. Sci. Lett. **393**, 159 (2014).
[24] M. Pozzo and D. Alfè, SpringerPlus **5**, 256 (2016).
[25] L. V. Pourovskii, J. Mravlje, A. Georges, S. I. Simak, and I. A. Abrikosov, New J. Phys. **19**, 073022 (2017).
[26] L. V. Pourovskii, J. Mravlje, M. Pozzo, and Alfè, Nat. Commun. **11**, 4105 (2020).
[27] J. Xu, P. Zhang, K. Haule, J. Minar, S. Wimmer, H. Ebert, and R. E. Cohen, Phys. Rev. Lett. **121**, 096601 (2018).
[28] F. Wagle and G. Steinle-Neumann, Geophys. J. Int. **213**, 237 (2018).
[29] J.A. Korell, M. French, G. Steinle-Neumann, and R. Redmer, Phys. Rev. Lett. **122**, 086601 (2019).
[30] M. Pozzo, C. Davies, D. Gubbins, and D. Alfè, Phys. Rev. B **87**, 014110 (2013).
[31] M. Pozzo, C. Davies, and D. Alfè, Earth Planet. Sci. Lett. **584**, 117466 (2022).
[32] A. Kietzmann, R. Redmer, M. P. Desjarlais, and T. R. Mattsson, Phys. Rev. Lett. **101**, 070401 (2008).
[33] M. French and T. R. Mattsson, Phys. Rev. B **90**, 165113 (2014).
[34] M. P. Desjarlais, J. D. Kress, and L. A. Collins, Phys. Rev. E **66**, 025401(R) (2002).
[35] B. B. L. Witte, M. Shihab, S. H. Glenzer, and R. Redmer, Phys. Rev. B **95**, 144105 (2017).
[36] P. Hohenberg and W. Kohn, Phys. Rev. **136**, B864 (1964).
[37] W. Kohn and L. J. Sham, Phys. Rev. **140**, A1133 (1965).
[38] N. D. Mermin, Phys. Rev. **137**, A1441 (1965).
[39] M. Born and R. Oppenheimer, Ann. Phys. **389**, 457 (1927).
[40] G. Kresse and J. Furthmüller, Phys. Rev. B **54**, 11169 (1996).
[41] G. Kresse and J. Hafner, Phys. Rev. B **47**, 558 (1993).
[42] G. Kresse and J. Hafner, Phys. Rev. B **49**, 14251 (1994).
[43] J. P. Perdew, K. Burke, and M. Ernzerhof, Phys. Rev. Lett. **77**, 3865 (1996).
[44] P. E. Blöchl, Phys. Rev. B **50**, 17953 (1994).
[45] G. Kresse and D. Joubert, Phys. Rev. B **59**, 1758 (1999).
[46] M. Valiev and J. H. Weare, J. Phys. Chem. A **103**, 10588 (1999).
[47] A. Baldereschi, Phys. Rev. B **7**, 5212 (1973).
[48] G. Steinle-Neumann, L. Stixrude, and R. E. Cohen, Proc. Natl. Acad. Sci. **101**, 33 (2004).
[49] C. X. Li, Key Eng. Mater. **837**, 146 (2020).
[50] S. Nosé, J. Chem. Phys. **81**, 511 (1984).
[51] W. G. Hoover, Phys. Rev. A **31**, 1695 (1985).
[52] B. Holst, M. French, and R. Redmer, Phys. Rev. B **83**, 235120 (2011).
[53] M. French and R. Redmer, Phys. Plasmas **24**, 092306 (2017).
[54] M. Gajdoš, K. Hummer, G. Kresse, J. Furthmüller, and F. Bechstedt, Phys. Rev. B **73**, 045112 (2006).
[55] R. Kubo, J. Phys. Soc. Jpn. **12**, 570 (1957).
[56] D. A. Greenwood, Proc. Phys. Soc. **71**, 585 (1958).
[57] See Supporting Material at http://link.aps.org/supplemental/10.1103/PhysRevB.107.085145 for convergence tables and additional figures.
[58] G. Wiedemann and R. Franz, Ann. Phys. **165**, 497 (1853).
[59] L. Lorenz, Ann. Phys. Chem. **223**, 429 (1872).
[60] A. Sommerfeld and H. Bethe, *Elektronentheorie der Metalle* (Springer, Berlin, 1967).
[61] H. J. Monkhorst and J. D. Pack, Phys. Rev. B **13**, 5188 (1976).
[62] D. Alfè, M. Pozzo, and M. P. Desjarlais, Phys. Rev. B **85**, 024102 (2012).
[63] C. M. S. Gannarelli, D. Alfè, and M. J. Gillan, Phys. Earth Planet. Inter. **152**, 67 (2005).
[64] G. Steinle-Neumann, L. Stixrude, and R. E. Cohen, Phys. Rev. B **60**, 791 (1999).
[65] K. Kádas, L. Vitos, and R. Ahuja, Earth Planet. Sci. Lett. **271**, 221 (2008).
[66] A. Dewaele, P. Loubeyre, F. Occelli, M. Mezouar, P. I. Dorogokupets, and M. Torrent, Phys. Rev. Lett. **97**, 215504 (2006).
[67] E. Edmund, F. Miozzi, G. Morard, E. Boulard, A. Clark, F. Decremps, G. Garbarino, V. Svitlyk, M. Mezouar, and D. Antonangeli, Minerals **10**, 98 (2020).
[68] Y. Ma, M. Somayazulu, G. Shen, H. Mao, J. Shu, and R. J. Hemley, Phys. Earth Planet. Inter. **143-144**, 455 (2004).
[69] J. Li, Q. Wu, J. Li, T. Xue, Y. Tan, X. Zhou, Y. Zhang, Z. Xiong, Z. Gao, and T. Sekine, Geophys. Res. Lett. **47**, e2020GL087758 (2020).
[70] K. Ohta, Y. Nishihara, Y. Sato, K. Hirose, T. Yagi, S. I. Kawaguchi, N. Hirao, and Y. Ohishi, Front. Earth Sci. **6**, 176 (2018).
[71] M. French, G. Röpke, M. Schörner, M. Bethkenhagen, M. P. Desjarlais, and R. Redmer, Phys. Rev. E **105**, 065204 (2022).
[72] S. S. Lobanov, Z. M. Geballe, Geophys. Res. Lett. **49**, e2022GL100379 (2022).
[73] A. B. Belonoshko, Condens. Matter Phys. **13**, 23605 (2010).
[74] J. B. van Zytveld, J. Phys. Colloques **41**, C8-503 (1980).
[75] R. S. Hixson, M. A. Winkler, and M. L. Hodgdon, Phys. Rev. B **42**, 6485 (1990).

[76] M. Beutl, G. Pottlacher, and H. Jäger, Int. J. Thermophys. **15**, 1323 (1994).

[77] K. C. Mills, B. J. Monaghan, and B. J. Keene, Int. Mater. Rev. **41**, 209 (1996).

[78] T. Nishi, H. Shibata, Y. Waseda, and H. Ohta, Metall. Mater. Trans. A **34**, 2801 (2003).

[79] L. Spitzer and R. Härm, Phys. Rev. **89**, 977 (1953).

[80] M. Lasbleis and R. Deguen, Phys. Earth Planet. Int. **247**, 80 (2015).

[81] F. Wagle, G. Steinle-Neumann, and N. de Koker, Comptes Rendus Geoscience **351**, 154 (2019).

[82] R. Deguen and P. Cardin, Geophys. J Int. **187**, 1101 (2011).

[83] A. Rivoldini, T. V. Hoolst, and O. Verhoeven, Icarus **201**, 12 (2009).

[84] I. Wardinski, H. Amit, B. Langlais, and E. Thébault, J. Geophys. Res. Planets **126**, e2020JE006792 (2021).

[85] A. Rivoldini and T. Van Hoolst, Earth Planet. Sci. Lett. **377-378**, 62 (2013).

[86] S. A. Hauck II, J.-L. Margot, S. C. Solomon, R. J. Phillips, C. L. Johnson, F. G. Lemoine, E. Mazarico, T. J. McCoy, S. Padovan, S. J. Peale, M. E. Perry, D. E. Smith, and M. T. Zuber, J. Geophys. Res. Planets **118**, 1204 (2013).